Geometric frustration of Jahn-Teller order and ice rules in the infinite-layer lattice

Woo Jin Kim (wjk316@stanford.edu)
Department of Applied Physics, Stanford University, Stanford
Michelle Smeaton
Department of Materials Science and Engineering, Cornell University
Chunjing Jia
SLAC and Stanford University https://orcid.org/0000-0001-7999-1932
Berit Goodge
Cornell University https://orcid.org/0000-0003-0948-7698
Byeong-Gwan Cho
Pohang Accelerator Laboratory
Kyuho Lee
kyuho@stanford.edu https://orcid.org/0000-0002-0817-0499
Motoki Osada
Stanford University
Anton Ievlev
Center for Nanophase Materials Sciences Oak Ridge National Laboratory
Brian Moritz
Lena Kourkoutis
Cornell University https://orcid.org/0000-0002-1303-1362
Thomas Devereaux
SLAC National Accelerator Laboratory https://orcid.org/0000-0001-8072-9237
Harold Hwang
Stanford University https://orcid.org/0000-0002-9230-3214

Physical Sciences - Article

Keywords:

Posted Date: April 6th, 2022

DOI: https://doi.org/10.21203/rs.3.rs-1524274/v1

Geometric frustration of Jahn-Teller order and ice rules in the infinite-layer lattice

Woo Jin Kim[1,2*], Michelle A. Smeaton[3], Chunjing Jia[1], Berit H. Goodge[4,5], Byoung-Gwan Cho[6], Kyuho Lee[1,7], Motoki Osada[1,8], Anton V. Ievlev[9], Brian Moritz[1], Lena F. Kourkoutis[4,5], Thomas P. Devereaux[1,8], and Harold Y. Hwang[1,7*]

[1] *Stanford Institute for Materials and Energy Sciences, SLAC National Accelerator Laboratory, Menlo Park, CA 94025, United States.*

[2] *Department of Applied Physics, Stanford University, Stanford, CA 94305, United States.*

[3] *Department of Materials Science and Engineering, Cornell University, Ithaca, NY 14853, United States*.

[4] *School of Applied and Engineering Physics, Cornell University, Ithaca, NY 14853, United States.*

[5] *Kavli Institute at Cornell for Nanoscale Science, Cornell University, Ithaca, NY 14853, United States.*

[6] *Pohang Accelerator Laboratory, POSTECH, Pohang, Gyungbuk 790-784, Republic of Korea.*

[7] *Department of Physics, Stanford University, Stanford, CA 94305, United States.*

[8] *Department of Materials Science and Engineering, Stanford University, Stanford, CA 94305, United States.*

[9] *Center for Nanophase Materials Sciences Oak Ridge National Laboratory, Oak Ridge, TN 37831, United States.*

[*]Correspondence to: wjk316@stanford.edu, hyhwang@stanford.edu

Abstract

The Jahn-Teller effect, in which electronic configurations with energetically degenerate orbitals induce lattice distortions to lift this degeneracy, plays a key role in many symmetry-lowering crystal deformations[1]. Lattices of Jahn-Teller ions can induce a cooperative distortion, as exemplified by $LaMnO_3$ (refs.[2–4]). While many examples occur in octahedrally[5] or tetrahedrally[6] coordinated transition metal oxides due to their high orbital degeneracy, this effect has yet to be manifested for square-planar coordination, as found in infinite-layer Cu (refs.[7–9]), Ni (refs.[10–12]), Fe (refs.[13–15]), and Mn oxides[16]. Here we synthesize single-crystal $CaCoO_2$ thin films by topotactic reduction of the Brownmillerite $CaCoO_{2.5}$ phase. We observe a dramatically distorted infinite-layer structure, with Angstrom-scale displacements of the cations from their high-symmetry positions. This can be understood to originate from the Jahn-Teller degeneracy of the d_{xz} and d_{yz}-orbitals in the d^7 electronic configuration along with substantial ligand-transition metal mixing. A complex pattern of distortions arises in a $2\sqrt{2} \times 2\sqrt{2} \times 1$ tetragonal supercell, reflecting the competition between an ordered Jahn-Teller effect of the CoO_2 sublattice, and geometric frustration of the associated displacements of the Ca sublattice. As a result of this competition, the $CaCoO_2$ structure forms an extended two-in/two-out type of Co distortion following "ice rules"[17].

The cooperative Jahn-Teller effect (JTE) often induces strong coupling between charge, orbital, and magnetic ordering, which has been related to many correlated phenomena such as colossal magnetoresistance[18,19] and superconductivity[20]. For the magnetoresistance associated with the metal-insulator transition in perovskite-based manganites, it has been established that the double-exchange model for magnetism cannot solely account for the large resistivity drop below the paramagnetic to ferromagnetic phase transition, and rather that a strong electron-phonon interaction arising from the JTE plays a crucial role[21–24]. Moreover, single-layered perovskite $(La,A)_2CuO_4$ (A: Sr and Ba) shows unconventional superconductivity within Jahn-Teller (JT)-distorted CuO_6 octahedra, indicating the important role of the JTE in many correlated ground states[25].

Despite its generality, the study of the cooperative JTE in oxides has been largely confined to octahedral and tetrahedral coordination. In perovskites, octahedral-site cations having outer-electron configurations of d^4, d^7 or d^9 (ref.[5]) are often JT-active systems, splitting the partially filled e_g-orbitals (Fig. 1a). In $LaMnO_3$ with high-spin state d^4, the partially filled e_g orbitals of Mn^{3+} induces both MnO_6 octahedral distortion (i.e. the Q_3-JT-distortion)[1] and d_{z2}-orbital ordering to reduce its total energy (Fig. 1b), resulting in an orthorhombic crystal structure (Fig. 1c). The cooperative JTE has also been observed in spinel structures with tetrahedral-site cations having d^1 or d^9 configurations[6]. The JTE in a square-planar configuration has been theoretically discussed from the foundations of the concept: that a Q_2 vibrational mode will distort the high-symmetry square coordination to a low-symmetry rhombus[1]. However, a pure cooperative Q_2-JT-distortion has yet to be experimentally observed in crystalline materials.

The infinite-layer structure provides a unique platform to explore this possibility, and the potential cooperative response in a lattice of JT ions. This structure forms a four-

coordinated transition metal oxide with a two-dimensional (2D) square lattice, which can often be derived from precursor higher oxides by de-intercalating the apical oxygen using topotactic reduction (Fig. 2a). These 2D oxides have been first synthesized in powder nickelates with extremely low nickel valence state (Ni^{+1}) (ref.[10]). The same four-coordinate system has also been found in copper oxide superconductors[7–9]. Subsequently, the iron oxide infinite-layer structure was discovered with antiferromagnetic ground states[13–15]. And recently, the hole-doped infinite-layer nickelates with Ni-3$d^{9-\delta}$ were found to be superconducting[26–28].

Within this quasi-2D structure, how the orbital degeneracy affects the crystal and electronic structure is an open experimental question. The crystal field structure for the square plane is quite different from those of octahedral or tetrahedral coordination, with lower overall degeneracy. As shown in Fig. 1d, only the d_{xz} and d_{yz}-orbitals are degenerate. Therefore, to be JT-active, the system should have a partially filled d_{xz} (or d_{yz}) orbital state. The high-spin d^7 configuration meets these conditions, making the infinite-layer cobaltates with Co^{2+} oxidation state an ideal candidate. Considering only the CoO_2 plane, one might expect a cooperative JTE to induce an orbitally-ordered lattice of d_{xz} or d_{yz}-orbital states in analogy to $LaMnO_3$ (Fig. 1e). As we will demonstrate, the collective response is considerably richer.

Angstrom-scale cation displacements in $CaCoO_2$

Here we stabilized a new infinite-layer compound $CaCoO_2$ with dramatic in-plane lattice distortions. The starting point is the synthesis of epitaxial single crystal thin films of brownmillerite $CaCoO_{2.5}$ on $SrTiO_3$ (001) substrates [see Methods; θ–2θ symmetric x-ray diffraction (XRD) scan Fig. 2b][29]. The high-angle annular dark-field (HAADF) scanning transmission electron microscopy (STEM) image of $CaCoO_{2.5}$ (Fig. 2d) confirms the excellent crystallinity with abrupt interfaces with the substrate and subsequent $SrTiO_3$ capping layer, which is used to stabilize the reduced phase. The $CaCoO_{2.5}$ heterostructure was then reduced

using CaH_2, after which the XRD symmetric scan only shows peaks corresponding to the infinite-layer structure (00*l*) (Fig. 2c), with a significant contraction of the out-of-plane lattice parameter from ~ 3.72 Å to c_t ~ 3.27 Å. From reciprocal space mapping (RSM), we extract the in-plane lattice constant a_t of $CaCoO_2$ to be ~ 3.86 Å (Extended Data Fig. 1), indicating that the reduced film is relaxed from the substrate.

The large *c*-axis difference between $CaCoO_2$ and $CaCoO_3$ closely follows trends of known infinite layer oxides (Extended Data Fig. 2)[30]. Furthermore, electron energy-loss spectroscopy of $CaCoO_2$ (Extended Data Fig. 3) is consistent with Co^{2+} (ref.[31]). Note that $SrCoO_2$ has been previously synthesized by reduction from $SrCoO_{2.5}$ (ref.[32]). However, $SrCoO_2$ has a much larger c_t (~ 3.76 Å) with tetrahedrally coordinated Co^{2+} - i.e., a fundamentally different structure[32]. Moreover, chemical characterization by time-of-flight secondary ion mass spectrometry (ToF-SIMS) shows no sign of hydrogen intercalation in $CaCoO_2$ (Extended Data Fig. 4), unlike structures such as $SrCoO_xH_y$[33-35]. To the best of our knowledge, the infinite layer structure we observe has not previously been reported for cobalt oxides.

The HAADF-STEM image along the $SrTiO_3$ [100] zone axis (Fig. 2e) shows that $CaCoO_2$ has a very strong in-plane superlattice modulation, unlike all known infinite-layer systems[7,11,13,28,36–38]. A closer look at the $CaCoO_2$ layer along the $[010]_t$-direction in Fig. 2f shows that this is due to in-plane cation displacements from the simple tetragonal infinite-layer structure. These are more clearly visible along the $[-110]_t$ axis (Fig. 2g), which reveals that both Co and Ca ions have alternating sites with very large splitting of 1.08 and 0.86 Å, respectively. Beyond these significant in-plane distortions, there are no observable accompanying out-of-plane atomic distortions (Extended Data Fig. 5). The θ–2θ asymmetric XRD scan also rules out a possible *c*-lattice doubling (Extended Data Fig. 6). In aggregate, these results show that the cation lattice is described by a tetragonal supercell $2\sqrt{2}a_t \times 2\sqrt{2}a_t$

$\times c_t$ ($a = b = 2\sqrt{2}a_t = 10.78$ Å and $c = c_t = 3.27$ Å) in the $P42_12$ symmetry group as shown in Fig. 2h (see Extended Data Table 1 for atomic coordinates). The projections of this crystal structure are shown in Fig. 2f and 2g, in close correspondence with the STEM images.

Structural refinement of the oxygen positions in $CaCoO_2$

Given the extremely small sample volume and low relative x-ray and electron scattering cross-sections for oxygen, determining their positions is quite challenging. Nevertheless, we can refine the oxygen positions from high-resolution synchrotron grazing incidence XRD (GIXRD) of the in-plane superlattice diffraction peaks (Fig. 3a). Using the cation coordinates from STEM, we first simulated the XRD pattern to find the seven strongest in-plane superlattice peaks (Extended Data Table 2) assuming undistorted oxygen positions[39]. These were then used to experimentally search for the actual scattering peaks, all of which were found very close to the simulated positions (Fig. 3b; Extended Data Table 2), confirming the overall structural symmetry deduced from the STEM results. The relative intensities of these peaks (blue diamonds in Fig. 3c) were then Rietveld refined (see Methods, Extended Data Table 3 and 4). The resulting refined crystal structure for $CaCoO_2$ is shown in Fig. 3d, which fits the GIXRD data very well (orange circles in Fig. 3c). The refinement was dominated by oxygen displacements, such that the initial R-factor of ~ 0.46 with undistorted oxygen (green squares in Fig. 3c) reduced to $R \sim 0.08$, indicative of a high-quality fit.

The plan-view HAADF-STEM image in Fig. 3e shows that the overlaid $CaCoO_2$ refined structure is in good agreement with the measurement results. The fast Fourier transform of the image (Fig. 3f) also confirms the existence of the seven in-plane peaks observed from the GIXRD measurements. The approximate oxygen positions can also be imaged via plan-view annular bright-field (ABF)-STEM. Figure 3g and h show that the refined structure of $CaCoO_2$

is a good qualitative match with the experimental results within the precision of the ABF-STEM measurement.

Origin of the ordered distortions in $CaCoO_2$

Figure 4a highlights the three distinct CoO_4 plaquettes (for $Co_{(1)}$, $Co_{(2)}$, and $Co_{(3)}$, coordinated by three distinct oxygen sites) in blue, green, and orange respectively for the refined structure of $CaCoO_2$. The blue $Co_{(1)}O_4$ plaquette shows strong JT-distortion as predicted[1]: the bonding length between $Co_{(1)}$ and $O_{(2)}$ ($d_{Co(1)-O(2)}$) is 2.22 $\pm$ 0.01 Å while that of $Co_{(1)}$ and $O_{(3)}$ ($d_{Co(1)-O(3)}$) is 1.13 $\pm$ 0.01 Å. Note that the anisotropic bonding ratio $d_{Co(1)-O(2)}/d_{Co(1)-O(3)}$ (1.96 $\pm$ 0.02) is extraordinarily large, for example compared to the value for the JT-distorted octahedra in $LaMnO_3$ (~ 1.15) (refs.[2,4]). The green $Co_{(2)}O_4$ plaquette is trapezoidal with three different Co-O bonding lengths, while that for $Co_{(3)}$ (orange) maintains 4-fold symmetry (with rotation). Surprisingly, only 25% of the Co is strongly JT-distorted, in contrast to the cooperative JTE in $LaMnO_3$ that provides an equivalent JT-octahedral distortion for every Mn site (Fig. 1c).

This intriguing situation can be understood to originate from the competition between the JT-distortion and an induced geometrical frustration in the Ca-layer. As shown by the dashed rectangles in Fig. 4a, the strong JTE distorts not only $Co_{(1)}O_4$ but also the Ca-layer. This unusual coupling of Ca to the Q_2-JT-distortion arises from the lack of apical oxygen, which gives rise to strong electrostatic coupling between the CoO_2 and Ca layers. The anisotropic distortions of the Ca-layer are however highly geometrically frustrated between neighboring sites (Fig. 1f). Consequently, a complex arrangement of displacements is observed.

Interestingly, the geometrical frustration of the cooperative JTE results in a two-in/two-out type of distortion pattern, following "ice rules"[17] for the angstrom-scale displacements of

$Co_{(2)}$ around the maximally JT-distorted $Co_{(1)}O_4$ (Fig. 4a). The $Co_{(2)}O_4$ plaquette notably breaks inversion symmetry, and thus the long-range ordered structure can be viewed as an ordering of electric dipoles. From an electrostatic point of view, this is equivalent to a "Herringbone" arrangement of electric quadrupoles (Fig. 4b), which minimizes the electrostatic interaction between quadrupole moments[40].

To further understand $CaCoO_2$, we performed density functional theory (DFT) + U calculations, as shown in Fig. 4c for the relaxed structure with U = 5 eV. The overall symmetry directly matches the experimental observations, and it is robust to variations in U (Extended Data Fig. 7). However, the magnitude of the distortions is significantly smaller – for example, the calculated anisotropic bonding ratio ~ 1.06 is much less than the experimentally observed 1.96 ± 0.02. The electronic band structure of $CaCoO_2$ shows an insulating ground state with a bandgap energy of $E_g \sim 1.024$ eV (Extended Data Fig. 8). Experimentally, the resistivity exhibits insulating temperature dependence, with a transport activation gap of 0.337 ± 0.001 eV (Extended Data Fig. 8).

The spin-dependent partial density of states (PDOS) for $Co_{(1)}$ shows that the d_{z2}- and d_{xz}-orbitals are doubly occupied (Fig. 4d) as expected from strong JT-splitting in a square planar geometry (absence of apical ligands), and the d_{yz}-orbital opens a gap between occupied and unoccupied states as indicated earlier (Fig. 1e). Overall, $Co_{(1)}$ is in a d^7 configuration where a spin down hole resides in both the d_{x2-y2}- and d_{xy}-orbitals, with an additional spin down hole in d_{yz}-orbitals (Figs. 1d and 4d). On the other hand, the spin-dependent PDOS for $Co_{(3)}$ sites show degenerate d_{xz}- and d_{yz}-orbitals due to the square symmetry of $Co_{(3)}O_4$ (Extended Data Fig. 9). These results are consistent with expectations from the simple crystal field structure in Fig. 1e, indicating that the JTE, together with electron correlations, drives the symmetry-lowering distortion and lifts the orbital degeneracy.

The quantitative discrepancy in the scale of distortions between experiment and theory may indicate the presence of large molecular orbital effects in this system that are difficult to capture using one-electron approaches[41-43]. Unlike octahedrally coordinated d^4 systems, the Q_2-JT-distortion, which splits the $d_{xz/yz}$ orbitals, draws the ligands along one direction inward, toward $Co_{(1)}$. This substantially increases the hybridization of the σ-bonded $Co_{(1)}$-O orbitals (Fig. 4a), encouraging a strong admixture of holes on the neighboring oxygen. Evidence for this tendency can be seen in the electron density distribution computed using the experimentally refined atomic positions (yellow isosurface in Fig. 4a), which is much more extended with significant weight on oxygen when compared to the computationally relaxed structure (yellow isosurface in Fig. 4c). Thus a "negative charge transfer" material may result, with trimerized molecular orbitals of Co ($3d_{x2-y2}$)-O ($2p_x$) hybrids, transitioning from high-spin Co $3d^7$ to a low-spin state Co $3d^8\underline{L}$, where $\underline{L}$ denotes a ligand hole dispersed among the neighboring σ-bonded oxygens (Fig. 4e). In fact, this could be the driving force behind the observed quadrupolar ordering (Fig. 4b).

Performing a small cluster exact diagonalization calculation for an 11-orbital unit cell (5-Co $3d$ and 3-O $2p_{x,y}$ orbitals; see Methods, result shown in Fig. 4f) confirms this picture. While a small JT-splitting gives the DFT-relaxed configuration (high-spin $3d^7$), increasing the hybridization between Co and O along one direction, as in the experimental structure, draws electron weight from O $2p_y$ to Co $3d_{x2-y2}$ (Fig. 4f), raising the $3d_{x2-y2}$ complex above the $3d_{xy/xz}$ orbitals, further reducing the degeneracy. This low-spin $3d^8\underline{L}$ configuration is common to other Co-based negative charge transfer systems such as $SrCoO_3$ (refs.[44-46]) but may be more easily achievable in a square planar environment. As the other less JT-distorted Co sites essential remain in a local high-spin JT-split $3d^7$ configuration, further local magnetic and X-ray scattering measurements may be extremely insightful.

Conclusion

In summary, we have found $CaCoO_2$ to be a model system for realizing the 2D JT lattice. In contrast to perovskite-based systems, the interlayer coupling between the Ca-layer and CoO_2 layer is strong such that the distorted structure is governed by the underlying competition between the JTE and the geometric frustration induced in the Ca-layer. This leads to a complex pattern of distortions that arise in a $2\sqrt{2}a_t \times 2\sqrt{2}a_t \times c_t$ unit cell and significant ligand-transition metal mixing. The understanding of the JTE here may have general implications for understanding complex compounds with 2D atomic layers where the JTE is prominent.

Methods

Synthesis of $CaCoO_2$ thin films

Brownmillerite $CaCoO_{2.5}$ thin films were synthesized by pulsed laser deposition (PLD) on perovskite $SrTiO_3$ (001) substrates. We used a $CaCoO_{2.5}$ polycrystalline target and a KrF excimer laser (λ = 248 nm, pulse repetition rate of 3 Hz, and laser fluence of 1 J/cm^2). The distance between the target and the substrate was maintained at ~ 50 mm. The optimal conditions for high-quality $CaCoO_{2.5}$ films were found to be a substrate temperature T = 600 °C under oxygen partial pressure P_{O2} = 50 mTorr. To protect the cobaltate films from potential degradation during and after the reduction process, we capped the as-grown $CaCoO_{2.5}$ with 5-unit cells of $SrTiO_3$. The precursor $CaCoO_{2.5}$ film was then reduced to $CaCoO_2$ by topotactic reduction. We loosely covered the $CaCoO_{2.5}$ film with aluminum foil and sealed it with ~ 0.1 g of CaH_2 powder in a vacuum glass tube. We annealed the sealed tube at 250 °C for 3 hours in a tube furnace. The thermal ramping and cooling rates were 10 °C/min.

Scanning transmission electron microscopy measurements

STEM specimens were prepared using a Thermo Fisher Scientific Helios G4 UX focused ion beam (FIB). Cross-section samples were prepared and thinned to electron transparency using standard lift out and thinning methods. Plan-view samples were prepared first using the standard lift out method and then attached to a half grid at a 90° angle to the standard orientation and thinned. Total air exposure of the prepared STEM specimens was limited to less than 15 minutes to minimize possible degradation of the films.

HAADF and ABF-STEM data were acquired using a Thermo Fisher Scientific Spectra 300 X-CFEG operating at 120 or 300 kV with a convergence angle of 30 mrad. Inner and outer collection angles were approximately 60 and 200 mrad respectively for HAADF and 15 and 30 mrad respectively for ABF imaging. To obtain high signal-to-noise-ratio (SNR) images, many fast-acquisition images were acquired and subsequently aligned using a rigid registration process optimized for noisy images[47]. Due to electron beam sensitivity of the sample, a probe current of less than 30 pA was used for all STEM data acquisitions. EELS measurements therefore required total acquisition times of ~5,000 seconds for each spectrum to achieve sufficient SNR to distinguish differences in the EELS fine structure. The spectra presented are aligned and summed series of several acquisitions. To ensure stage stability sufficient for such long acquisitions, a Nion UltraSTEM operated at 100 kV and equipped with a high stability stage, an Enfinium ER spectrometer, and Quefina2 camera was used to acquire all EELS data. The effective energy resolution, measured by the full-width-at-half-maximum of the zero-loss peak, was ~ 0.34 eV. To ensure consistency, spectra from multiple regions of each sample were acquired. Each individual spectrum was aligned in energy based on the well-studied $SrTiO_3$ Ti-$L_{3,2}$ edge recorded while scanning over both substrate and film. Aligned spectra were summed to produce high SNR measurements of the Co-$L_{3,2}$ and Ca-$L_{3,2}$ edges for the as-grown and reduced films. White line ratios were calculated from the Co-$L_{3,2}$ edges using the Pearson method.

Synchrotron Grazing Incidence X-ray Diffraction

The synchrotron grazing incidence X-ray diffraction (GIXRD) experiments were performed at room temperature (293 K) using the Huber six-circle diffractometer at 3A beamline of the Pohang Light Source-II in South Korea. The incident beam from an undulator source was

monochromatized to 1.1078 Å. The Incident beam angle was fixed to 0.2°. The synchrotron XRD data were collected in a 2θ range from 0° to 75° with a step interval of 0.01°.

GIXRD refinement

The GIXRD peaks were analyzed by the Rietveld method. We used the least-squares method to minimize the function $M = \sum_i \{I_i^{obs} - I_i^{calc}\}^2$, where I_i^{obs} and I_i^{calc} are the observed and calculated integrated Bragg peak intensity of the i^{th} (*hkl*) plane. We used seven independent (*hkl*) planes for the refinement. The calculated Bragg peak intensity for the (*hkl*) plane is given as $I_{hkl}^{calc} = Kp_{hkl}L_\theta|F_{hkl}|^2$, where K, p_{hkl}, L_θ, and F_{hkl} are the scaling factor, number of equivalent (*hkl*)-planes, Lorentz polarization factor, and structure form factor, respectively. We used the *R*-factor, $R = \frac{\sum_i |I_i^{obs} - I_i^{calc}|}{\sum_i I_i^{obs}}$, to quantify the goodness of fit.

Sample characterization

The conventional XRD data were taken using a monochromatized Cu $K\alpha_1$ source (λ = 1.5406 Å). The resistivity was measured using Al wire bonded contacts in a Hall bar geometry.

Time of flight secondary ion mass spectrometry (ToF-SIMS)

ToF-SIMS characterization was performed using TOF.SIMS.5 NSC instrument (ION.TOF Gmb, Germany). Primary Bi^+ ion beam with energy of 30 keV, DC current of 30 nA and spot size ~5 μm was used for extraction of the secondary ions of the analyzed sample. Complimentary Cs^+ sputtering beam with energy of 500 eV and current of 40 nA was used for depth profiling. A low energy unfocused electron flood gun was used for charge compensation. Measurements were performed in non-interlaced mode, where each scan with Bi^+ (100 by 100 μm, 4 s duration) was followed by a sputtering cycle with Cs^+ (300 by 300 μm, 2s duration). A time of flight mass analyzer operated in positive ions mode was used to analyze

secondary ions with mass resolution $m/\Delta m$ = 2,000 – 5,000. The acquired chemical data provide 1D depth profiles, characterizing the distribution of the elements of interest through the sample thickness. Depth calibration was performed using the known sample thickness in the assumption of homogenous sputter rates.

DFT + U calculations

The initial structure was taken with all the atoms positioned at high symmetry points of the simple tetragonal structure with a $2\sqrt{2}a_t \times 2\sqrt{2}a_t \times 2c_t$ supercell. Then structural relaxation was implemented with this initial structure using DFT + U calculations, where the PBE[48] exchange-correlation functional was used and DFT + U was treated using the simplified (rotationally invariant) approach introduced by Dudarev *et al*.[49]. All DFT + U calculations were performed using the Vienna *Ab initio* Simulation Package (VASP)[50]. The structural relaxation and self-consistent calculations were performed with 8 by 8 by 16 Monkhorst-Pack momentum points, while the density of states calculations were performed with 20 by 20 by 40 Monkhorst-Pack momentum points. Note that DFT + U calculations with various U values were explored, and 5 eV was chosen as the onset of opening a gap. The obtained relaxed structure shows the same structural symmetry breaking as found in the experimental structure but with smaller distortions. The magnitude and symmetry of the distortion are robust to variations in U values (Extended Data Fig. 7).

Cluster multiplet calculations

The calculations were performed via exact diagonalization of CoO_2 11-orbital cluster involving 5-Co 3*d* orbitals and 6-O 2*p* orbitals forming 90° bond angles. The Hubbard-Kanamori interaction for O and Co orbitals captures, multiplet energy levels parametrized by Slater-Condon integrals *F*. Hybridization is included via tight-binding hopping; charge transfer

energy Δ and crystal field levels ε are chosen to give a high-spin Co $3d^7$ ground state (total spin 3/2, 8-fold ground state degeneracy) for the undistorted plaquette. A Jahn-Teller perturbation that lifts the ground state degeneracy is applied by changing relative orbital energies for $3d_{xz/yz}$, which maintains the high-spin ground state, while reducing the degeneracy to 4. Increasing the hybridization (hopping) along the *x* bond directions reduces the degeneracy to 2 and creates a low-spin ground state characterized by $3d^8L$ with a ligand hole occupancy in the $2p_x$ orbital. Parameters are given in Extended Data Table 5.

Acknowledgments

The work at SLAC and Stanford was supported by the U.S. Department of Energy (DOE), Office of Basic Energy Sciences, Division of Materials Sciences and Engineering (contract No. DE-AC02-76SF00515) and the Gordon and Betty Moore Foundation's Emergent Phenomena in Quantum Systems Initiative (grant No. GBMF9072, synthesis equipment). Electron microscopy at Cornell was support by the Department of Defense Air Force Office of Scientific Research (No. FA 9550-16-1-0305) and the Packard Foundation, and made use of the Cornell Center for Materials Research Shared Facilities which are supported through the NSF MRSEC program (DMR-1719875), with the Thermo Fisher Helios G4 X FIB also support by NSF (DMR-1539918). M.A.S. acknowledges additional support from the NSF GRFP under award number DGE-1650441. 3A beamline at PLS-II is supported in part by MSIT. ToF-SIMS characterization was conducted at the Center for Nanophase Materials Sciences, which is a DOE Office of Science User Facility, and using instrumentation within ORNL's Materials Characterization Core provided by UT-Battelle, LLC under Contract No. DE-AC05-00OR22725. The computational work for this project was performed on the Sherlock cluster in the Stanford Research Computing Center.

Author contributions

W.J.K. and H.Y.H. conceived and designed the experiments. M.A.S., B.H.G., and L.F.K. performed the STEM measurements and analysis. C.J. performed the DFT calculations. C.J., B.M., and T.P.D. performed the cluster calculations. W.J.K. grew the samples, characterized by W.J.K., K.L, and M.O. W.J.K. and B.-G.C. performed and analyzed the synchrotron GIXRD measurements. A.V.I. performed ToF-SIMS measurements. W.J.K., T.P.D. and H.Y.H. wrote the manuscript, with input from all authors.

Competing financial interests

The authors declare no competing financial interests.

References

1. Jahn, H.A. and Teller, E. Stability of Polyatomic Molecules in Degenerate Electronic States. *Proc. R. Soc. London* **161**, 220–235 (1937).
2. Goodenough, J. B. Theory of the Role of Covalence in the Perovskite-Type Manganites [La,M(II)]MnO_3. *Phys. Rev.* **100**, 564–573 (1955).
3. Gehring, G. A. & Gehring, K. A. Co-operative Jahn-Teller effects. *Reports Prog. Phys.* **38**, 1–89 (1975).
4. Millis, A. J. Cooperative Jahn-Teller effect and electron-phonon coupling in $La_{1-x}A_xMnO_3$. *Phys. Rev. B* **53**, 8434–8441 (1996).
5. Goodenough, J. B. JAHN-TELLER PHENOMENA IN SOLIDS. *Annu. Rev. Mater. Sci.* **28**, 1–27 (1998).
6. Goodenough, J. B. Jahn-Teller distortions induced by tetrahedral-site Fe^{2+} ions. *J. Phys. Chem. Solids* **25**, 151–160 (1964).
7. Siegrist, T., Zahurak, S. M., Murphy, D. W. & Roth, R. S. The parent structure of the layered high-temperature superconductors. *Nature* **334**, 231–232 (1988).
8. Smith, M. G., Manthiram, A., Zhou, J., Goodenough, J. B. & Markert, J. T. Electron-doped superconductivity at 40 K in the infinite-layer compound $Sr_{1-y}Nd_yCuO_2$. *Nature* **351**, 549–551 (1991).
9. Azuma, M., Hiroi, Z., Takano, M., Bando, Y. & Takeda, Y. Superconductivity at 110 K in the infinite-layer compound $(Sr_{1-x}Ca_x)_{1-y}CuO_2$. *Nature* **356**, 775–776 (1992).
10. Crespin, M., Levitz, P. & Gatineau, L. Reduced forms of $LaNiO_3$ perovskite. Part 1.—Evidence for new phases: $La_2Ni_2O_5$ and $LaNiO_2$. *J. Chem. Soc., Faraday Trans. 2* **79**, 1181–1194 (1983).
11. Hayward, M. A., Green, M. A., Rosseinsky, M. J. & Sloan, J. Sodium Hydride as a Powerful Reducing Agent for Topotactic Oxide Deintercalation: Synthesis and

Characterization of the Nickel(I) Oxide $LaNiO_2$. *J. Am. Chem. Soc.* **121**, 8843–8854 (1999).

12. Hayward, M. A. & Rosseinsky, M. J. Synthesis of the infinite layer Ni(I) phase $NdNiO_{2+x}$ by low temperature reduction of $NdNiO_3$ with sodium hydride. *Solid State Sci.* **5**, 839–850 (2003).

13. Tsujimoto, Y. *et al.* Infinite-layer iron oxide with a square-planar coordination. *Nature* **450**, 1062–1065 (2007).

14. Kawakami, T. *et al.* Spin transition in a four-coordinate iron oxide. *Nat. Chem.* **1**, 371–376 (2009).

15. Tassel, C. *et al.* $CaFeO_2$: A New Type of Layered Structure with Iron in a Distorted Square Planar Coordination. *J. Am. Chem. Soc.* **131**, 221–229 (2009).

16. Dixon, E., Hadermann, J., Ramos, S., Goodwin, A. L. & Hayward, M. A. Mn(I) in an Extended Oxide: The Synthesis and Characterization of $La_{1-x}Ca_xMnO_{2+\delta}$ ($0.6 \leq x \leq 1$). *J. Am. Chem. Soc.* **133**, 18397–18405 (2011).

17. Pauling, L. The Structure and Entropy of Ice and of Other Crystals with Some Randomness of Atomic Arrangement. *J. Am. Chem. Soc.* **57**, 2680–2684 (1935).

18. von Helmolt, R., Wecker, J., Holzapfel, B., Schultz, L. & Samwer, K. Giant negative magnetoresistance in perovskitelike $La_{2/3}Ba_{1/3}MnO_x$ ferromagnetic films. *Phys. Rev. Lett.* **71**, 2331–2333 (1993).

19. Urushibara, A., Moritomo, Y., Arima, T., Asamitsu, A., Kido,G. & Tokura, Y. . Insulator-metal transition and giant magnetoresistance in $La_{1-x}Sr_xMnO_3$. *Phys. Rev. B* **51**, 14103 (1995).

20. Han, J. E., Gunnarsson, O. & Crespi, V. H. Strong Superconductivity with Local Jahn-Teller Phonons in C_{60} Solids. *Phys. Rev. Lett.* **90**, 167006 (2003).

21. Millis, A. J., Littlewood, P. B. & Shraiman, B. I. Double Exchange Alone Does Not

Explain the Resistivity of $La_{1-x}Sr_xMnO_3$. *Phys. Rev. Lett.* **74**, 5144–5147 (1995).

22. Millis, A. J., Shraiman, B. I. & Mueller, R. Dynamic Jahn-Teller Effect and Colossal Magnetoresistance in $La_{1-x}Sr_xMnO_3$. *Phys. Rev. Lett.* **77**, 175–178 (1996).

23. Röder, H., Zang, J. & Bishop, A. R. Lattice Effects in the Colossal-Magnetoresistance Manganites. *Phys. Rev. Lett.* **76**, 1356–1359 (1996).

24. Guzmán-Verri, G. G., Brierley, R. T. & Littlewood, P. B. Cooperative elastic fluctuations provide tuning of the metal–insulator transition. *Nature* **576**, 429–432 (2019).

25. Keller, H., Bussmann-Holder, A. & Müller, K. A. Jahn–Teller physics and high-T_c superconductivity. *Mater. Today* **11**, 38–46 (2008).

26. Li, D. *et al.* Superconductivity in an infinite-layer nickelate. *Nature* **572**, 624–627 (2019).

27. Li, D. *et al.* Superconducting Dome in $Nd_{1-x}Sr_xNiO_2$ Infinite Layer Films. *Phys. Rev. Lett.* **125**, 27001 (2020).

28. Zeng, S. *et al.* Phase Diagram and Superconducting Dome of Infinite-Layer $Nd_{1-x}Sr_xNiO_2$ Thin Films. *Phys. Rev. Lett.* **125**, 147003 (2020).

29. Boullay, P. *et al.* Structure determination of a brownmillerite $Ca_2Co_2O_5$ thin film by precession electron diffraction. *Phys. Rev. B* **79**, 184108 (2009).

30. Li, X. *et al.* Exceptional oxygen evolution reactivities on $CaCoO_3$ and $SrCoO_3$. *Sci. Adv.* **5**, eaav6262 (2019).

31. Wang, Z. L. & Yin, J. S. Cobalt valence and crystal structure of $La_{0.5}Sr_{0.5}CoO_{2.25}$. *Philos. Mag. B* **77**, 49–65 (1998).

32. Li, H.-B. *et al.* Dehydration of Electrochemically Protonated Oxide: $SrCoO_2$ with Square Spin Tubes. *J. Am. Chem. Soc.* **143**, 17517–17525 (2021).

33. Hayward, M. A. *et al.* The Hydride Anion in an Extended Transition Metal Oxide

Array: $LaSrCoO_3H_{0.7}$. *Science* **295**, 1882–1884 (2002).

34. Katayama, T. *et al.* Topotactic synthesis of strontium cobalt oxyhydride thin film with perovskite structure. *AIP Advances* **5**, 107147 (2015).

35. Lu, N. *et al.* Electric-field control of tri-state phase transformation with a selective dual-ion switch. *Nature* **546**, 124–128 (2017).

36. Lee, K. *et al.* Aspects of the synthesis of thin film superconducting infinite-layer nickelates. *APL Mater.* **8**, 41107 (2020).

37. Yamamoto, T. *et al.* Synthesis and Thermal Stability of the Solid Solution $AFeO_2$ (A = Ba, Sr, Ca). *Inorg. Chem.***49**, 5957–5962 (2010).

38. Osada, M. *et al.* Nickelate superconductivity without rare-earth magnetism: $(La,Sr)NiO_2$. *Adv. Mater.* **33**, 2104083 (2021).

39. Momma, K. and Izumi, F. VESTA: a three-dimensional visualization system for electronic and structural analysis. *J. Appl. Crystallogr.* **41**, 653–658 (2008).

40. Williams, J. H. The Molecular Electric Quadrupole Moment and Solid-State Architecture. *Acc. Chem. Res.* **26**, 593–598 (1993).

41. Radaelli, P. G. *et al.* Formation of isomorphic Ir^{3+} and Ir^{4+} octamers and spin dimerization in the spinel $CuIr_2S_4$. *Nature* **416**, 155–158 (2002).

42. Nguyen, L. T. *et al.* Geometrically frustrated trimer-based Mott insulator. *Phys. Rev. Materials* **2**, 054414 (2018).

43. Khomskii, D. I. and Streltsov, S. V. Orbital Effects in Solids: Basics, Recent Progress, and Opportunities. *Chem. Rev.* **121**, 2992–3030 (2021).

44. Potze, R. H., Sawatzky, G. A., and Abbate, M. Possibility for an intermediate-spin ground state in the charge-transfer material $SrCoO_3$. *Phys. Rev. B* **51**, 17 (1995).

45. Saitoh, T. *et al.* Electronic structure and magnetic states in $La_{1-x}Sr_xCoO_3$ studied by photoemission and x-ray-absorption spectroscopy. *Phys. Rev. B* **56**, 3 (1997).

46. Zhuang, M. *et al.* Possible magnetic ground state in the perovskite $SrCoO_3$. *Phys. Rev. B* **57**, 21 (1998).

47. Savitzky, B. H. *et al.* Image registration of low signal-to-noise cryo-STEM data. *Ultramicroscopy* **191**, 56-65 (2018).

48. Perdew, J. P *et al.* Generalized Gradient Approximation Made Simple. *Phys. Rev. Lett.* **77**, 3865 (1996).

49. Dudarev, S.L. *et al.* Electron-energy-loss spectra and the structural stability of nickel oxide: An LSDA+U study. *Phy. Rev. B* **57**, 1505 (1998).

50. Kresse, G. and Hafner, J. Ab initio molecular dynamics for liquid metals. *Phys. Rev. B* **47**, 558 (1993).

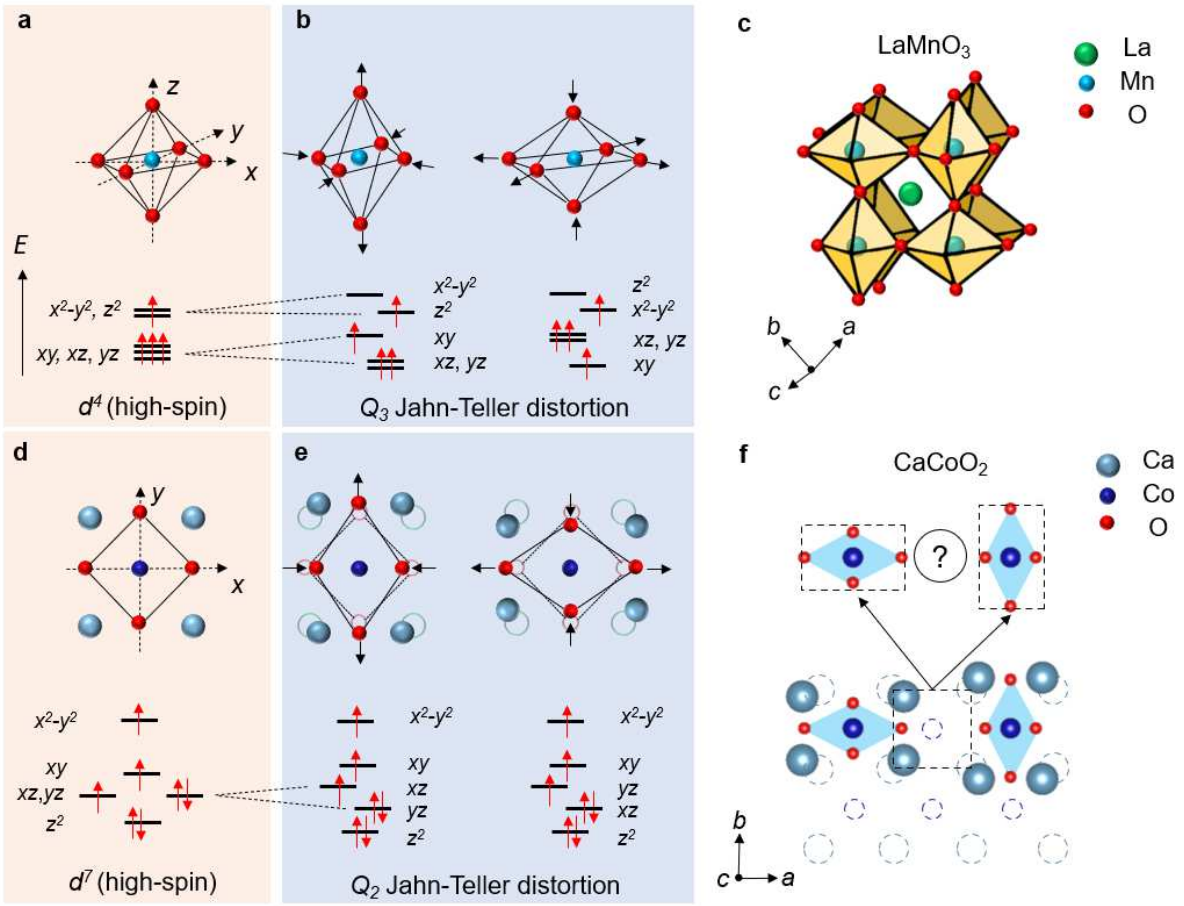

Figure 1 | Jahn-Teller distortion in three- and two-dimensional oxide lattices. a, Schematic MO_6 (M: transition metal) octahedron and crystal field structure for a high-spin d^4 electron configuration. **b**, Octahedral distortions and associated orbital levels for a Q_3-JT-distortion. **c**, Strong Q_3-JT-distorted $LaMnO_3$ crystal structure with high-spin d^4 Mn^{3+} as an example of a cooperative JT-distortion. **d**, Schematic square-planar MO_4 plaquette and crystal field structure for a high-spin d^7 electron configuration. **e**, Square-planar distortion and associated orbital levels for a Q_2-JT-distortion. **f**, Displacements in the Ca-layer geometrically frustrate a simple cooperative JT-distortion analogous to $LaMnO_3$.

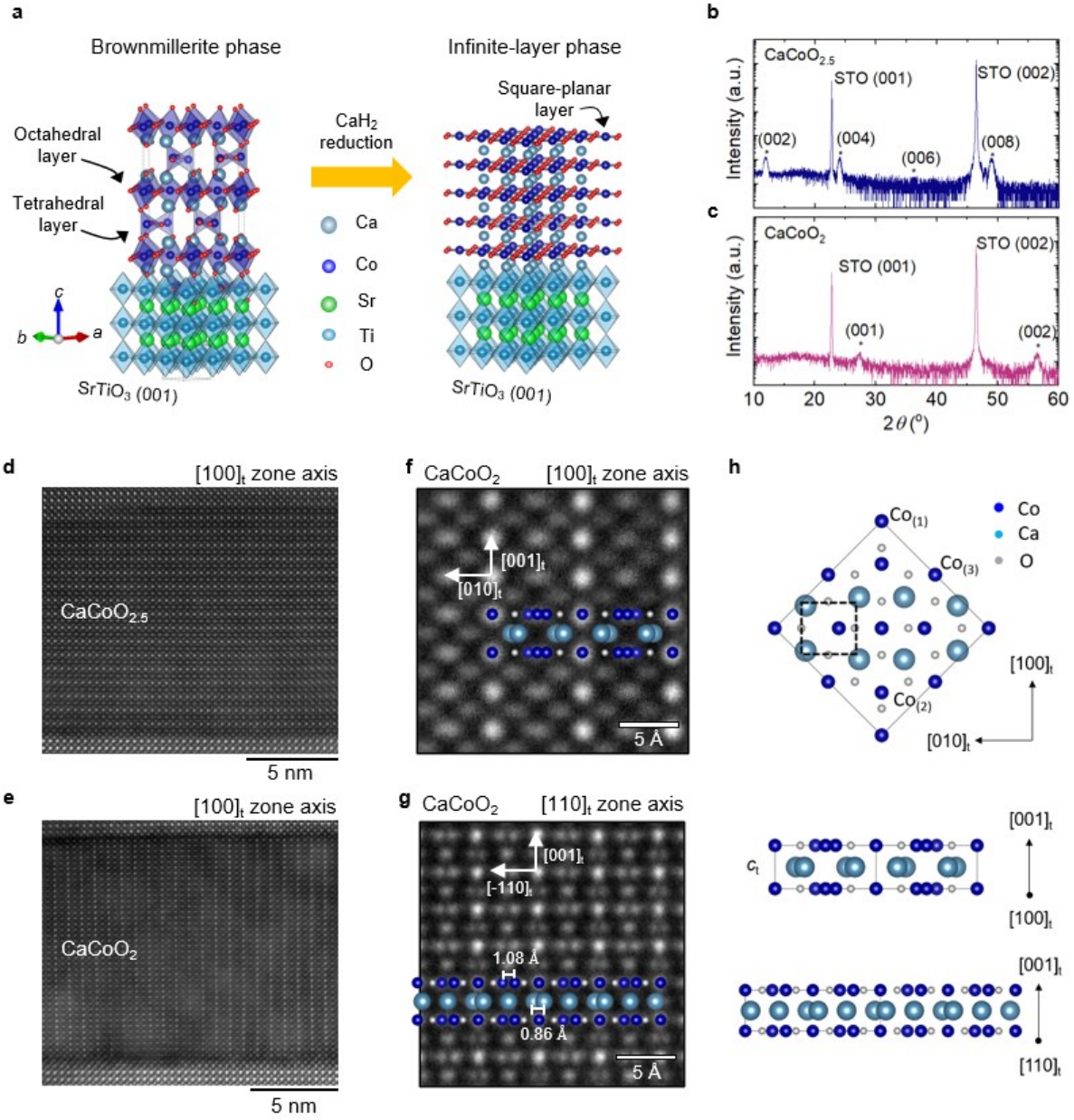

Figure 2 | Synthesis and large-scale cation displacements in thin film $CaCoO_2$. a, Schematic of the topotactic reduction of brownmillerite $CaCoO_{2.5}$ (left) to infinite-layer $CaCoO_2$ (right). XRD θ–2θ symmetric scans of **b**, 18-nm-thick $CaCoO_{2.5}$ and **c**, $CaCoO_2$ films capped with 2-nm-thick $SrTiO_3$ (STO) layers grown on $SrTiO_3$ (001) substrates. **d**, Atomic-resolution HAADF-STEM image taken along the $[100]_t$ zone-axis of $CaCoO_{2.5}$ which shows alternate stacking of tetrahedral and octahedral layers. **e**, HAADF-STEM image taken along the $[100]_t$ zone-axis of $CaCoO_2$. **f**, **g**, High-magnification HAADF-STEM images of $CaCoO_2$ taken along the $[100]_t$ and $[110]_t$ zone-axis, respectively. **h**, Unit cell structure of $CaCoO_2$ based on HAADF-STEM. Dark (bright) blue balls indicate Co (Ca) cations and grey balls indicate oxygen. The atomic positions of oxygen here are shown for the ideal square planar sites.

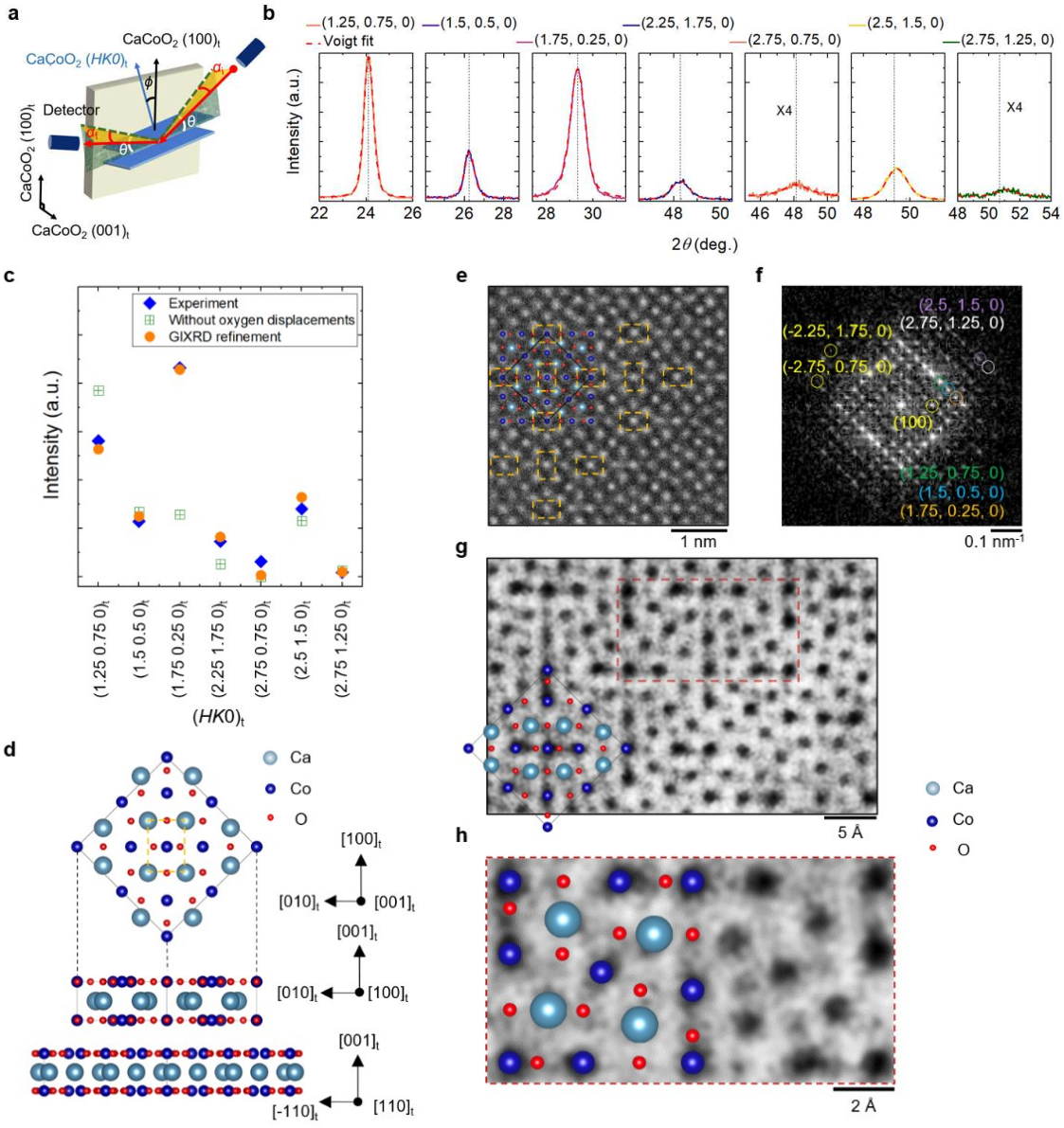

Figure 3 | GIXRD refinement and plan-view STEM. a, Schematic of the GIXRD experimental geometry. α_i and α_f are the incident and reflected angle, respectively, which are maintained to be 0.2° for all measurements. ϕ is the angle between $CaCoO_2$ $(100)_t$ and $(HK0)_t$ and θ is the diffraction angle for $CaCoO_2$ $(HK0)_t$ planes. **b**, GIXRD θ–2θ scans for various $CaCoO_2$ $(HK0)_t$ planes. The red dashed lines indicate Voigt fitting results. **c**, Relative integrated intensity for all $CaCoO_2$ $(HK0)_t$ GIXRD peaks. The blue (orange) filled diamonds (circles) are experimental (GIXRD refinement) results. The green crossed squares are calculated GIXRD intensity for $CaCoO_2$ in the absence of oxygen displacements (oxygen positions for an ideal square plane). **d**, GIXRD refined crystal structure for $CaCoO_2$. The red solid balls indicate the oxygen positions after refinement. **e**, Plan-view HAADF-STEM image of $CaCoO_2$. Atomic arrangements are consistent with the refined structure. The distorted Ca-layer is clearly seen in the image (yellow dashed rectangles). **f**, Fast Fourier transform of a larger field-of-view image including **e**. All seven peaks observed by GIXRD are captured. **g**, Plan-view ABF-STEM image of $CaCoO_2$ with refined structure model. Dark areas indicate the atomic positions. **h**, A magnified image of the region indicated by the dashed red rectangle in **g.**

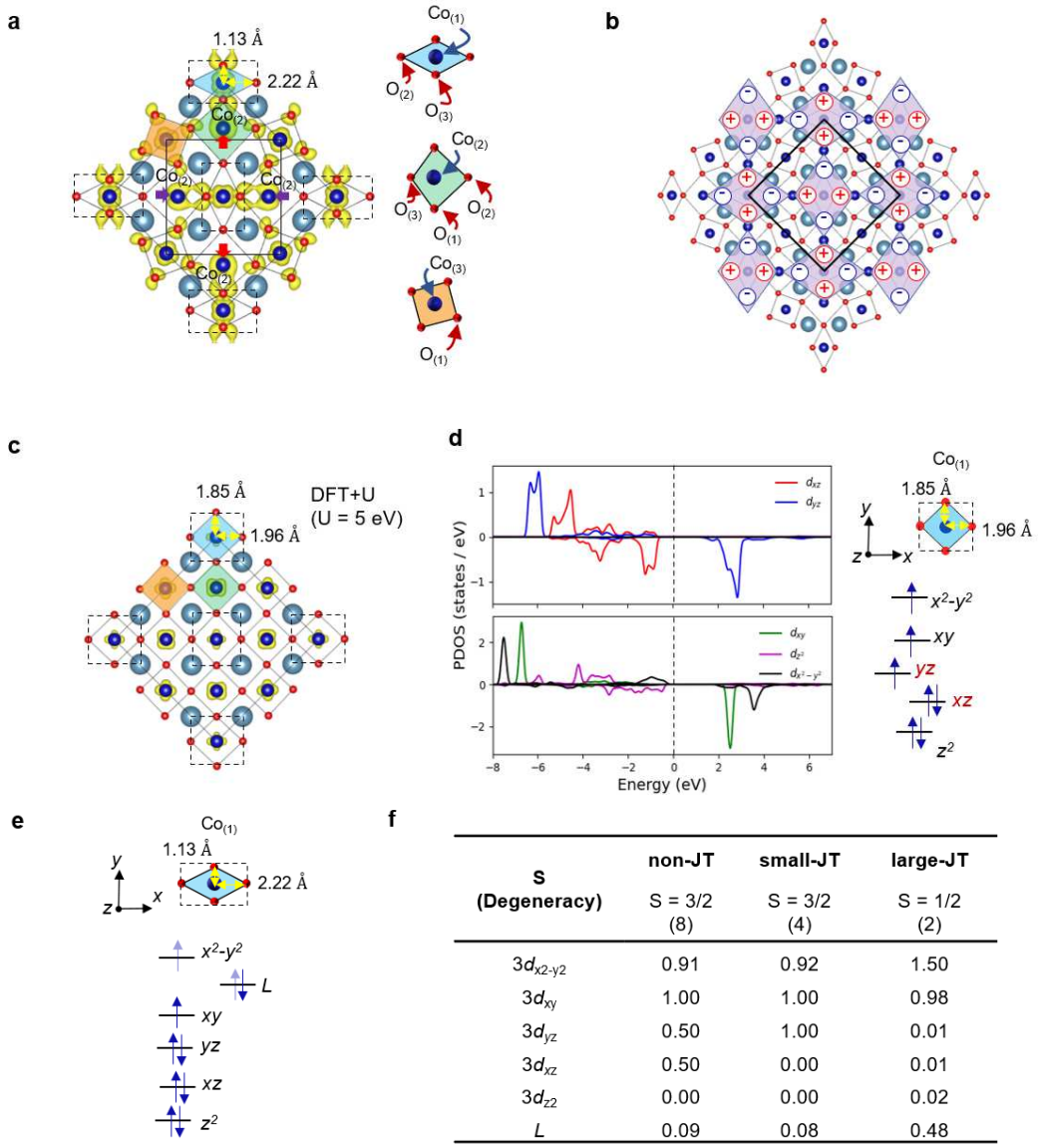

S (Degeneracy)	non-JT S = 3/2 (8)	small-JT S = 3/2 (4)	large-JT S = 1/2 (2)
$3d_{x2-y2}$	0.91	0.92	1.50
$3d_{xy}$	1.00	1.00	0.98
$3d_{yz}$	0.50	1.00	0.01
$3d_{xz}$	0.50	0.00	0.01
$3d_{z2}$	0.00	0.00	0.02
L	0.09	0.08	0.48

Figure 4 | Extended structure of $CaCoO_2$ – ice rules, quadrupolar ordering, and electronic structure. a, Planar-view of the experimentally-refined crystal structure of $CaCoO_2$, consisting of three different CoO_4 sites corresponding to the three different colors (blue, green, and orange). The blue-colored CoO_4 plaquettes are strongly JT-distorted. In the full unit cell, a pair of $Co_{(2)}$-ions distort toward (purple arrows) the central $Co_{(1)}$, while the other pair of $Co_{(2)}$-ions distort outward (red arrows) from the central $Co_{(1)}$. The visualized isosurface in yellow represents the computed electron density for the lowest unoccupied d_{x2-y2} band for $Co_{(1)}$ at the Gamma point. **b**, The dipole arrangements associated with $Co_{(2)}$ displacements form an ordered array of electric quadrupoles (purple diamonds). **c**, Planar-view of the computationally-relaxed crystal structure of $CaCoO_2$ from DFT + U (U = 5 eV) calculations. This consists of three different CoO_4 sites, which show the same structural symmetry as experiment, but with much smaller distortions. The visualized isosurface in yellow color represents the electron density for the lowest unoccupied d_{x2-y2} band for $Co_{(1)}$ at the Gamma point. **d**, The spin-dependent partial density of states of $Co_{(1)}$ *d*-orbitals from DFT + U and the corresponding atomic energy level diagram for the relaxed structure. **e**, An atomic energy level diagram appropriate for the experimentally-refined structure from a ligand-multiplet calculation. Light blue arrows represent the occupation of half an electron. **f**, A table showing the number of holes from ligand-multiplet calculations. The three columns give results in the absence of distortions (non-JT), for parameters appropriate for the DFT + U relaxed structure (small-JT), and for parameters appropriate for the experimentally-refined structure (large-JT).

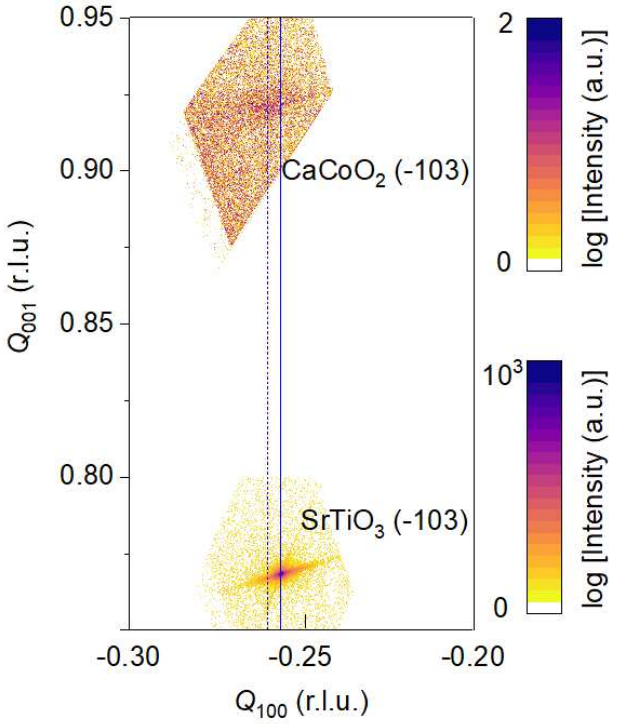

Extended Data Fig. 1 | X-ray diffraction reciprocal space mapping of thin film $CaCoO_2$. Reciprocal space map of $CaCoO_2$ around the (-103) $SrTiO_3$ diffraction peak, indicating that the film is relaxed from the substrate.

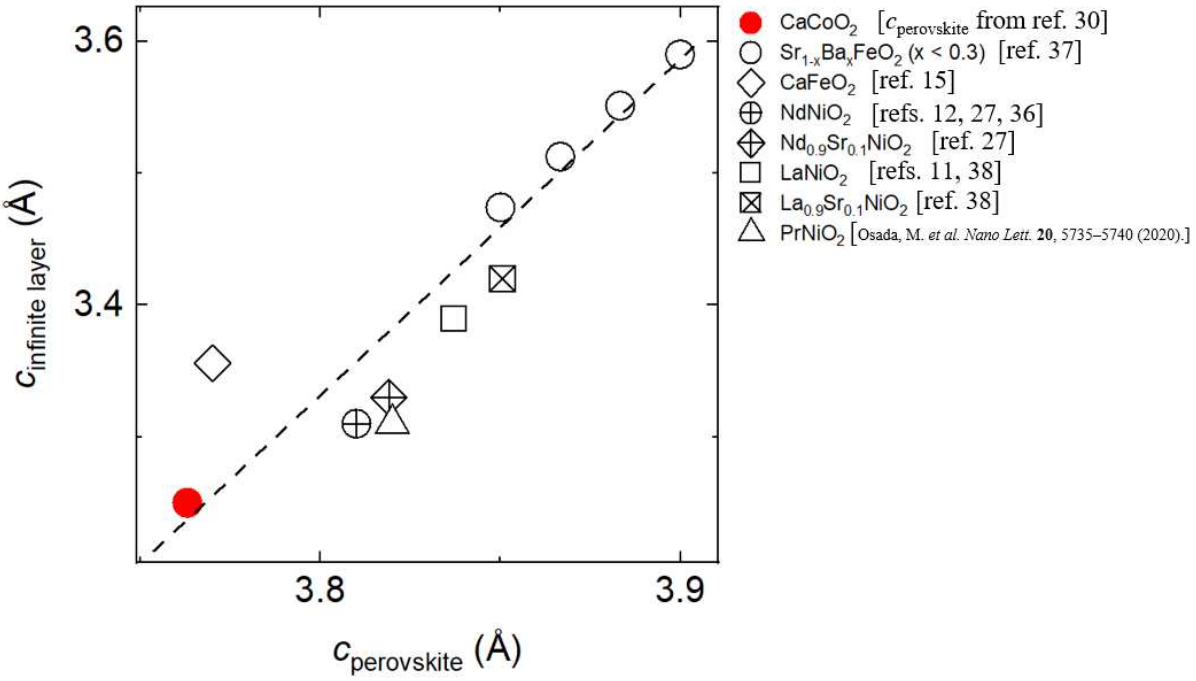

Extended Data Fig. 2 | Empirical relationship between perovskite and infinite layer lattice parameters. *c*-axis lattice parameters for various transition metal oxide compounds are plotted for the perovskite phase and the infinite-layer phase after topotactic reduction. The dashed line is a linear fit for all the data points in the plot. Note that the $CaFeO_2$ has relatively large $c_{infinite\ layer}/c_{perovskite}$ associate with out-of-plane displacement of both FeO_4 and Ca layers [ref.[15]].

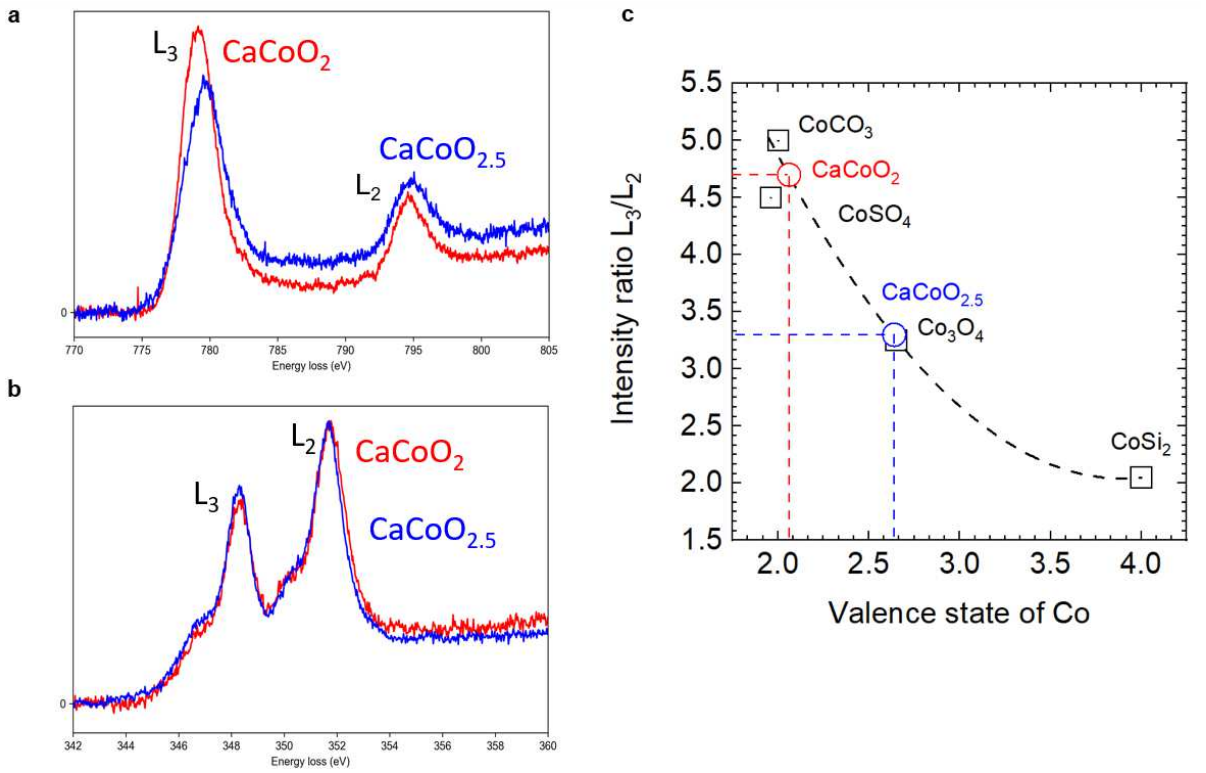

Extended Data Fig. 3 | EELS measurements of $CaCoO_2$. a, Co-$L_{3,2}$ edge; the blue (red) solid line indicates EELS spectra for $CaCoO_{2.5}$ ($CaCoO_2$). **b**, Ca-$L_{3,2}$ edge EELS shows that there are no significant changes of spectra before ($CaCoO_{2.5}$) and after reduction ($CaCoO_2$). **c**, A plot of the intensity ratio $I(L_3)/I(L_2)$ for different Co compounds with different oxidation states. Note that the dashed line indicates a polynomial fit curve for four different compounds from [ref.[31]] ($CoCO_3$, $CoSO_4$, Co_3O_4, and $CoSi_4$). $I(L_3)/I(L_2)$ of the $CaCoO_{2.5}$ and $CaCoO_2$ films are depicted with blue and red circles, respectively.

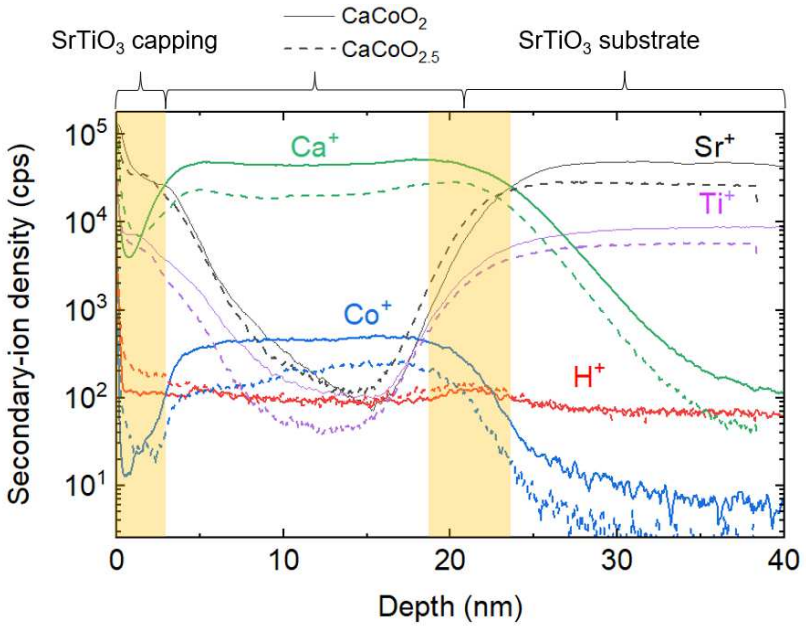

Extended Data Fig. 4 | Time-of-flight secondary-ion mass spectrometry (TOF-SIMS) measurement of thin film $CaCoO_2$. Depth profiles of H^+ and other ions from both $CaCoO_{2.5}$ and $CaCoO_2$ thin film on $SrTiO_3$ substrate (with ~ 2 nm $SrTiO_3$ capping layer) were measured with secondary-ion mass spectrometry. The Co ion signals from both $CaCoO_{2.5}$ and $CaCoO_2$ thin films were employed as a marker for the interface position. TOF-SIMS measurements show that the H^+ concentration for $CaCoO_2$ is similar to the background level of the as-synthesized $CaCoO_{2.5}$ thin film.

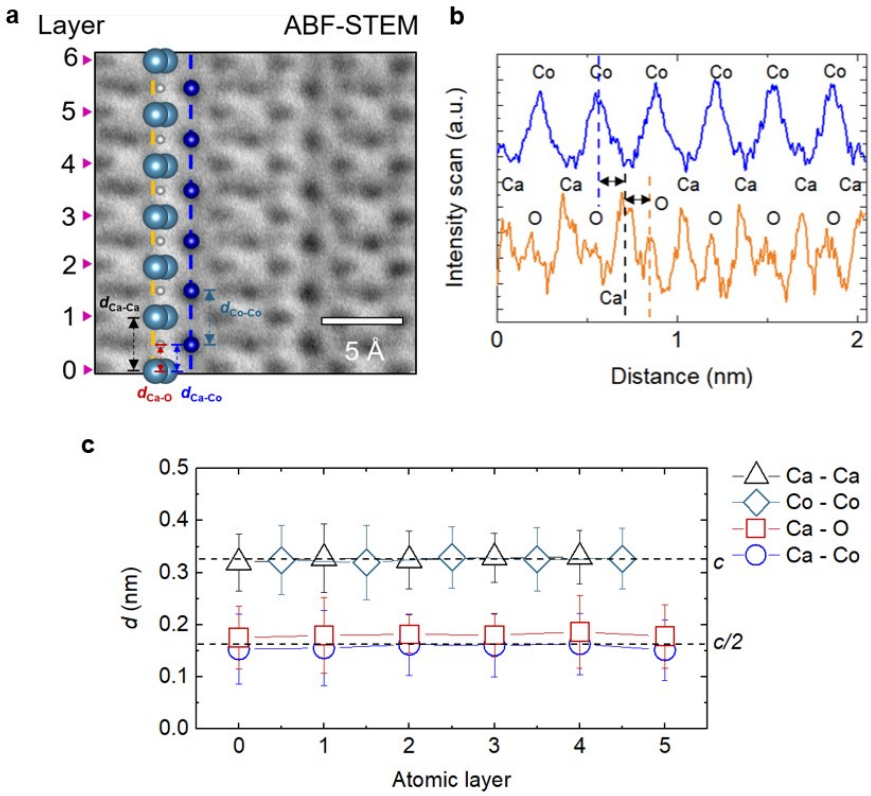

Extended Data Fig. 5 | ABF-STEM image of $CaCoO_2$. a, ABF-STEM imaging along the $[100]_t$ zone-axis with overlaid Co, Ca, and oxygen atoms. **b**, Intensity line profile for the blue and the orange dashed line in **a**. The intensities in the line profile are from inverted image **a**, and the blue (orange) solid line indicates the line profile for the Co column (Ca and oxygen column). The peak positions are the relative distance from the bottom of the image **a**. **c**, Atomic distances between Ca and Ca (black triangles), Co and Co (green diamonds), Ca and oxygen (red squares), and Ca and Co (blue circles) layer are plotted. Note that the atomic layer number in **c** correspond to that of in **a**, and the distance error bars are taken from the full-width-half-maximum of the intensity peaks in **b**.

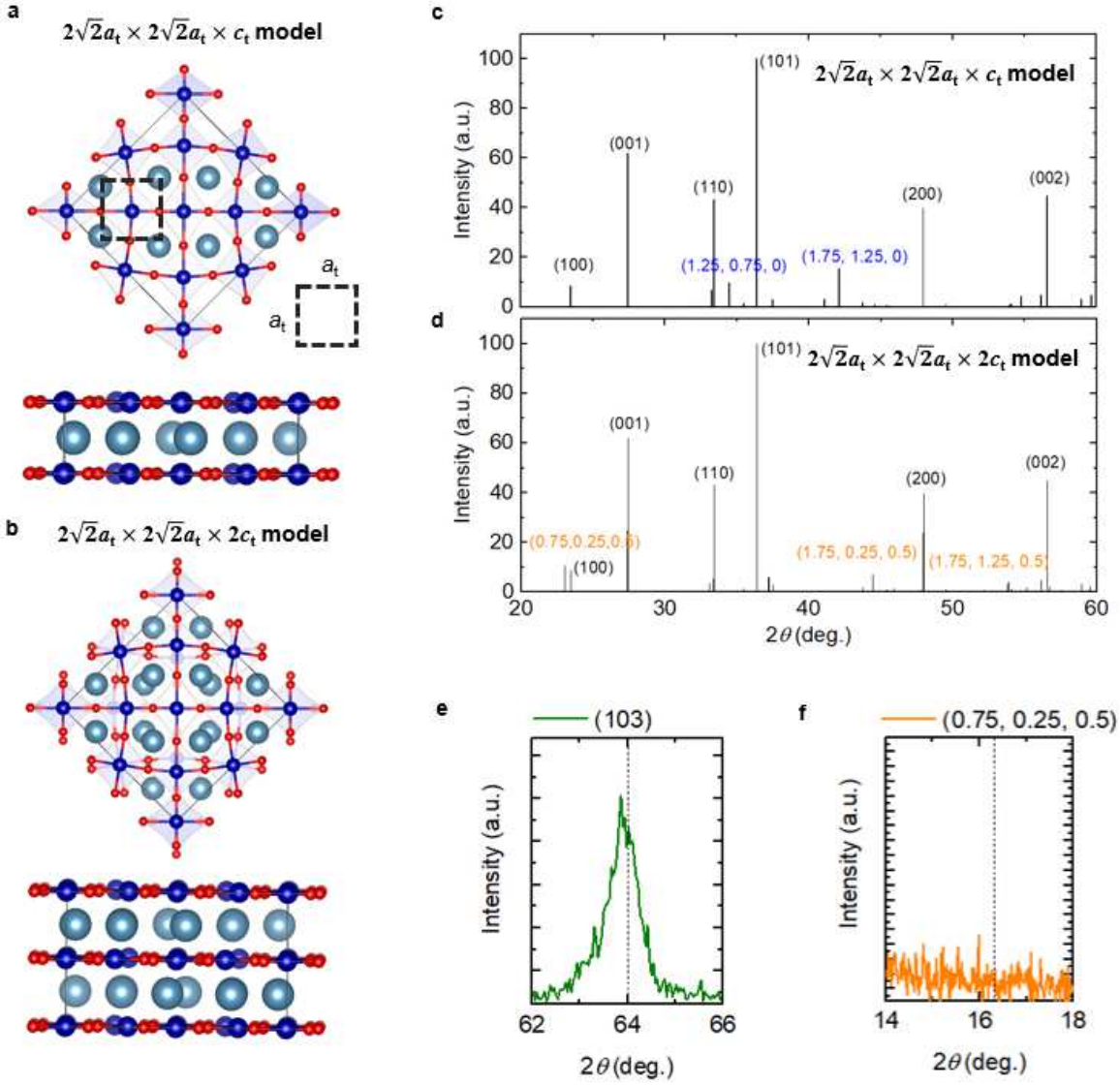

Extended Data Fig. 6 | Powder XRD simulation and *c*-lattice parameter determination. Lattice structure models for **a,** $2\sqrt{2}a_t \times 2\sqrt{2}a_t \times c_t$ and **b,** $2\sqrt{2}a_t \times 2\sqrt{2}a_t \times 2c_t$. The second structure model is lattice doubled from the first model by stacking a half-unit cell shifted layer along the in-plane direction. Powder XRD simulation results for both **c,** $2\sqrt{2}a_t \times 2\sqrt{2}a_t \times c_t$ and **d,** $2\sqrt{2}a_t \times 2\sqrt{2}a_t \times 2c_t$ models. Note that the XRD simulation for the $2\sqrt{2}a_t \times 2\sqrt{2}a_t \times 2c_t$ model has a distinct half-order peak along the *c*-lattice direction. We first found **e**, the $CaCoO_2$ $(103)_t$ XRD peak as a reference peak. Based on this reference peak position, we perform θ–2θ scans along the expected $CaCoO_2$ (0.75, 0.25, 0.5) position. **f**, No XRD peak was observed at the expected $CaCoO_2$ (0.75, 0.25, 0.5) peak position, indicating that $CaCoO_2$ does not have a *c*-axis doubling of the simple tetragonal unit cell.

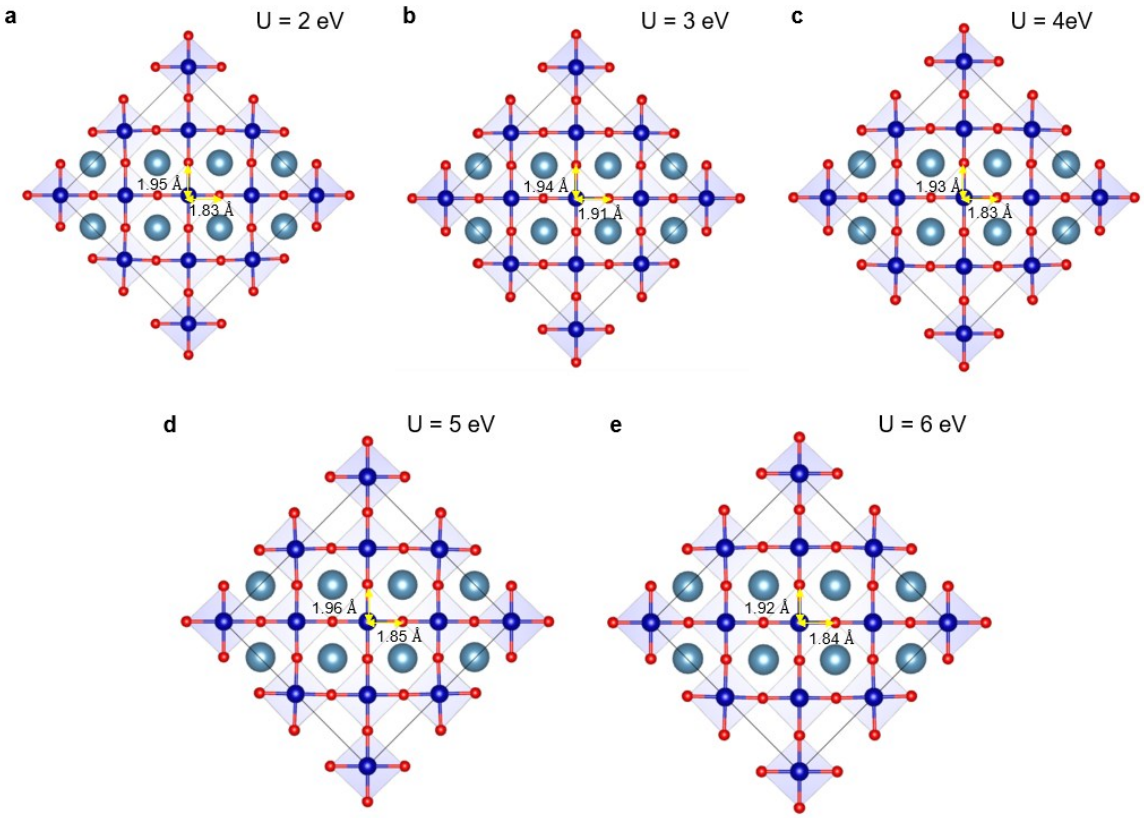

Extended Data Fig. 7 | $CaCoO_2$ DFT + U relaxed crystal structure with various U values. Planar-view of the relaxed crystal structure for $CaCoO_2$ from DFT + U calculations with **a**, U = 2 eV, **b**, U = 3 eV, **c**, U = 4 eV, **d**, U = 5 eV, and **e**, U = 6 eV.

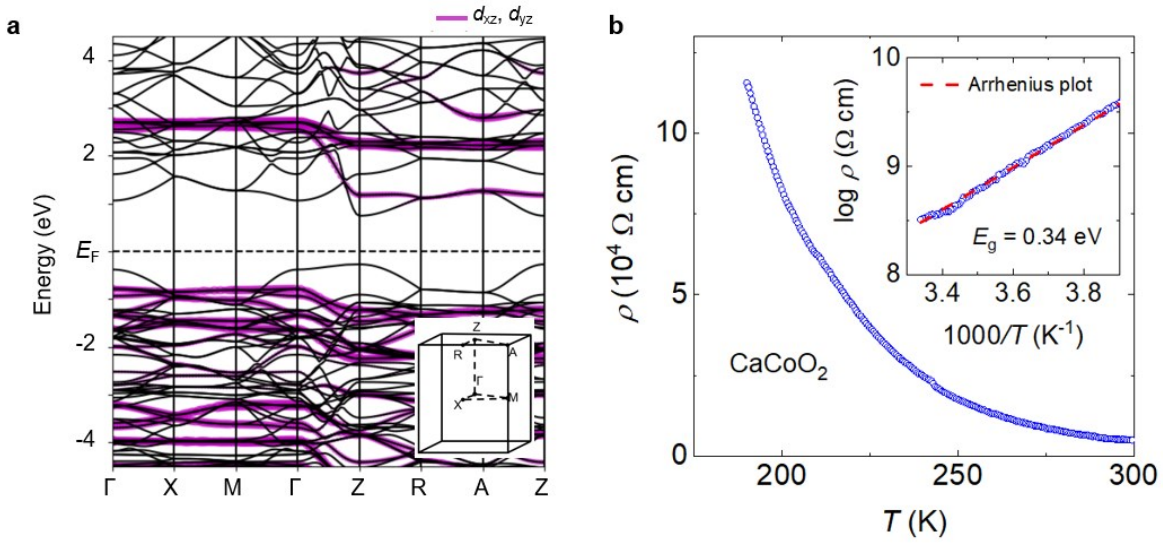

Extended Data Fig. 8 | Insulating phase of $CaCoO_2$ thin film. a, Calculated band dispersion of $CaCoO_2$ (DFT + U for U = 5 eV). Purple highlights d_{xz} (and d_{yz}) projections. The inset shows high symmetry points in the tetragonal Brillouin zone. **b,** Resistivity versus temperature of $CaCoO_2$ thin film. The inset shows that the resistivity is well fitted with an Arrhenius plot with an estimated (transport) gap energy of 0.337 $\pm$ 0.001 eV.

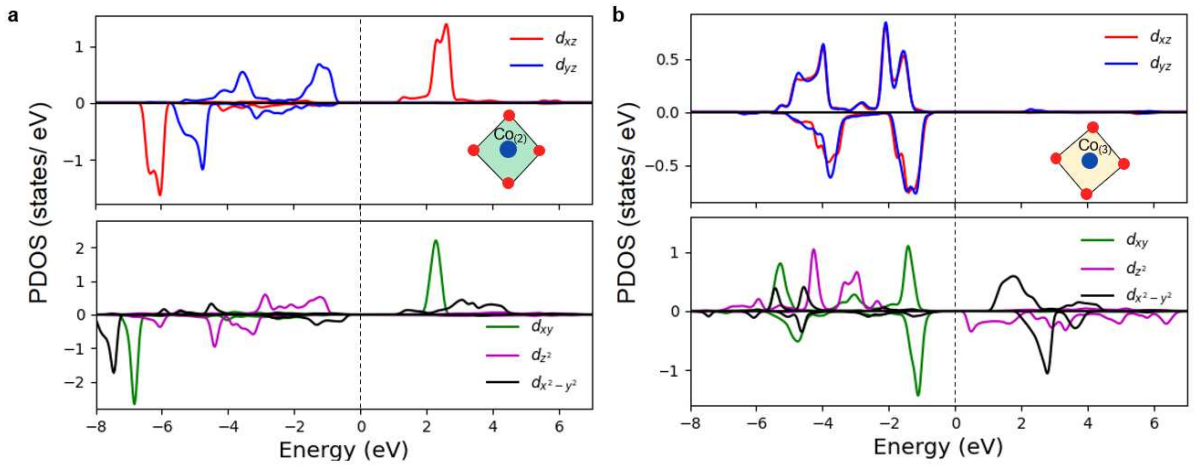

Extended Data Fig. 9 | The spin-dependent partial density of states for $Co_{(2)}$ and $Co_{(3)}$ for the computationally relaxed structure. a, The spin-dependent partial density of states (PDOS) of **a**, $Co_{(2)}$ and **b**, $Co_{(3)}$ *d*-orbitals from DFT + U (U = 5 eV). The spin-dependent PDOS of $Co_{(2)}$ shows the degeneracy lifting of the $d_{xz/yx}$-orbitals.

Extended Table 1 | Atomic coordinates for the cations in $CaCoO_2$ from HAADF-STEM.

$P42_12$ symmetry group

atom	x	y	z	occupation
$Co_{(1)}$	0	0	0	1
$Co_{(2)}$	0.2 ± 0.01	0.2 ± 0.01	0	1
$Co_{(3)}$	0.5	0	0	1
Ca	0.46 ± 0.01	0.25 ± 0.01	0.5	1

Extended Data Table 2 | Simulated and experimental $CaCoO_2$ $(HK0)_t$ GIXRD peak positions and intensities.

Photon energy 11.2 keV (0.11078 nm)

h	*k*	*l*	$\phi_{sim.}$ (°)	$\phi_{exp.}$ (°)	$2\theta_{sim.}$ (°)	$2\theta_{exp.}$ (°)	$Intensity_{sim.}$ (a.u.)	$Intensity_{exp.}$ (a.u.)
1.25	0.75	0	30.96	30.83 ± 0.002	24.47	24.10 ± 0.001	9.92	1406 ± 13
0.5	1.5	0	18.43	18.31 ± 0.002	26.58	26.24 ± 0.002	3.03	574 ± 10
1.75	0.25	0	8.13	7.72 ± 0.002	29.79	29.33 ± 0.002	15.10	2162 ± 20
2.25	1.75	0	37.88	37.74 ± 0.003	48.96	48.24 ± 0.004	5.04	366 ± 8
2.75	0.75	0	15.26	15.64 ± 0.032	48.96	48.14 ± 0.027	0.90	160 ± 29
2.5	1.5	0	30.96	31.02 ± 0.003	50.16	49.43 ± 0.003	3.48	704 ± 10
2.75	1.25	0	24.44	24.53 ± 0.035	52.10	51.10 ± 0.034	0.36	46 ± 7

Extended Data Table 3 | Atomic coordinates for the initial (before GIXRD refinement) and refined structure of $CaCoO_2$. Oxygen coordinates for the ideal simple-tetragonal infinite-layer structure were used for the initial simulation. VESTA software[39] was used.

$P42_12$ symmetry group

Atom	x		y		z		Occupation
	Initial	Refined	Initial	Refined	Initial	Refined	
$Co_{(1)}$	0	0	0	0	0	0	1
$Co_{(2)}$	0.200	0.205 ± 0.011	0.200	0.200 ± 0.011	0	0	1
$Co_{(3)}$	0.500	0.500	0	0	0	0	1
Ca	0.460	0.449 ± 0.012	0.250	0.250 ± 0.011	0.500	0.500	1
$O_{(1)}$	0.375	0.343 ± 0.013	0.125	0.125 ± 0.009	0	0	1
$O_{(2)}$	0.375	0.354 ± 0.012	0.375	0.354 ± 0.012	0	0	1
$O_{(3)}$	0.125	0.074 ± 0.011	0.125	0.074 ± 0.011	0	0	1

Extended Data Table 4 | Structure symmetry and atomic coordinates for the refined structure of $CaCoO_2$.

Data collection	**$CaCoO_2$ (GIXRD refinement)**				
Space group	$P42_12$ (No. 90)				
Cell dimensions					
a, *b*, *c* (Å)	$a = b = 10.78$ Å, $c = 3.27$ Å				
α, β, γ (°)	$\alpha = \beta = \gamma = 90^o$				
Atomic coordination	*Atom*	*x*	*y*	*z*	*Occupation*
	$Co_{(1)}$	0	0	0	1
	$Co_{(2)}$	0.205 ± 0.011	0.205 ± 0.011	0	1
	$Co_{(3)}$	0.500	0	0	1
	Ca	0.449 ± 0.012	0.245 ± 0.011	0.500	1
	$O_{(1)}$	0.343 ± 0.013	0.057 ± 0.009	0	1
	$O_{(2)}$	0.354 ± 0.012	0.354 ± 0.012	0	1
	$O_{(3)}$	0.074 ± 0.011	0.074 ± 0.011	0	1

Extended Data Table 5 | Parameters used for multiplet calculations (in eV). These parameters were used to generate the ground state ($3d^7$) configuration for the cluster. The high spin Jahn-Teller split ground state was obtained by lifting the degeneracy of the $e_{xz/yz}$ site energies, while the low spin ground state was obtained by increasing all hybridizations along the *x*-direction of the cluster.

F_0	6
F_2	0.12857
F_4	0.025
Coulomb U_{dd}	7.4
Hund's J	0.886
Average Coulomb $\bar{U}$	5.45
ε_{x2-y2}	0
ε_{z2}	2.4
ε_{xy}	0.2
$\varepsilon_{xz/yz}$	1.2
Δ	$3\bar{U}$
t_{pd}	1
t_{pdz}	$t_{pd}/4$
$t_{pdxy} = t_{pdxz} = t_{pdyz}$	0.225
$t_{pp\sigma}$	0.25
Coulomb U_{pp}	1

Data availability. The data that support the plots within this paper and other finding of this study are available from the corresponding author on reasonable request.